

Article

## Chemistry of the $\text{Fe}_2\text{O}_3/\text{BiFeO}_3$ Interface in $\text{BiFeO}_3$ Thin Film Heterostructures

Miryam Arredondo <sup>1</sup>, Quentin M. Ramasse <sup>2</sup>, Kashinath Bogle <sup>1</sup> and Valanoor Nagarajan <sup>1,\*</sup>

<sup>1</sup> School of Materials Science and Engineering, University of New South Wales, Sydney NSW 2052, Australia; E-Mails: arredond@mpi-halle.mpg.de (M.A.); kashinath.bogle@unsw.edu.au (K.B.)

<sup>2</sup> SuperSTEM Laboratory, STFC Daresbury, Keckwick Lane, Daresbury WA4 4AD, UK; E-Mail: qmramasse@superstem.org

\* Author to whom correspondence should be addressed; E-Mail: nagarajan@unsw.edu.au; Tel.: +61-2-9385-4263; Fax: +61-2-9385-5956.

Received: 10 November 2010; in revised form: 2 December 2010 / Accepted: 13 December 2010 / Published: 14 December 2010

---

**Abstract:** We investigate the interfacial chemistry of secondary  $\text{Fe}_2\text{O}_3$  phases formed in a  $\text{BiFeO}_3$  (BFO) layer in  $\text{BFO}/\text{La}_{0.67}\text{Sr}_{0.33}\text{MnO}_3$  (LSMO)/ $\text{SrTiO}_3$  (STO) heterostructures. A combination of high-resolution spherical aberration corrected scanning TEM and spectroscopy results, reveals that specific chemical and crystallographic similarities between  $\text{Fe}_2\text{O}_3$  and BFO, enable the BFO layer to form a facile host for  $\text{Fe}_2\text{O}_3$ .

**Keywords:** multiferroic  $\text{BiFeO}_3$ ; perovskite; Z-contrast imaging; EELS

---

### 1. Introduction

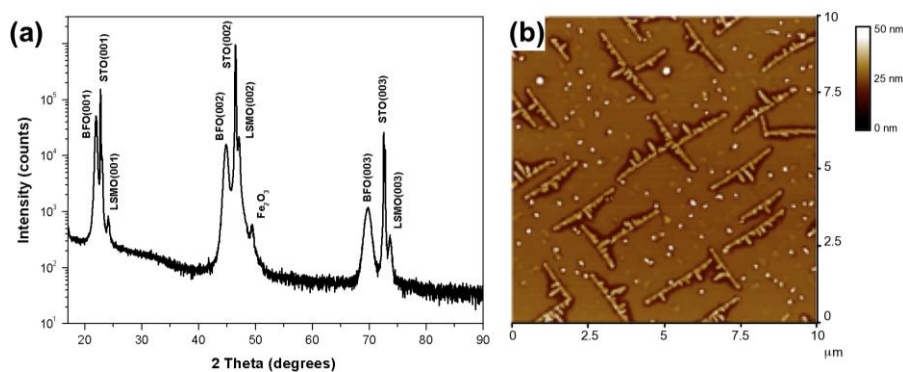
Perovskite Bismuth Iron Oxide ( $\text{BiFeO}_3$ , BFO) has attracted immense interest in recent times as, not only, a multiferroic [1,2] but also a Pb-free piezoelectric candidate, with attractive electromechanical properties [3,4]. However, Bismuth (Bi) is quite similar to Lead (Pb) in terms of its chemical stability—it is volatile under high temperatures and vacuum. Consequently, BFO thin film deposition requires the use of Bi-excess targets or precursors to compensate for the Bi loss at nominally employed high growth temperatures [5]. Moreover BFO has a very narrow thin film deposition window to obtain phase pure BFO thin films, which necessitates a rigid control in terms of the precursor chemistry, temperature and oxygen pressure, to synthesize the films. For example,

incorrect Bi concentration in the targets can create secondary phases, such as  $\text{Fe}_2\text{O}_3$  [6,7], while improper oxygen environments during laser ablation can lead to pockets of  $\text{Bi}_2\text{O}_3$  [6]; on the other hand, high growth temperatures can also lead to cation diffusion across the thin film interfaces [8]. Additionally, it has been found that oxygen vacancies could induce significant leakage current [9,10]. Among the secondary phases that can be created during the BFO deposition process, there has been a significant interest in  $\text{Fe}_2\text{O}_3$  phases found in BFO thin films. A highly controversial issue is whether or not parasitic  $\text{Fe}_2\text{O}_3$  is the primary reason for enhancement of magnetic properties in BFO [2]. The presence of the  $\text{Fe}_2\text{O}_3$  phase also complicates the study of BFO thin films [6,11] as a model multiferroic material. On the other hand, studies have shown that  $\text{Fe}_2\text{O}_3$  embedded in BFO can be considered to be a new type of multiferroic nanocomposite material [7]. For example, it has been reported that the presence of  $\alpha$ - and  $\gamma$ - $\text{Fe}_2\text{O}_3$  phases enhances the BFO strain relaxation and magnetization [9]. These previous reports on the associated impact of  $\text{Fe}_2\text{O}_3$  on the properties of BFO, claim that detailed high-resolution studies are needed in order to understand the nature of the interface between the  $\text{Fe}_2\text{O}_3$  phase and the BFO film. The objective of this study is to understand the chemical and structural features of an interface between BFO and  $\text{Fe}_2\text{O}_3$  and, hence, reveal why this system is so facile for such nanocomposite synthesis.

## 2. Results and Discussion

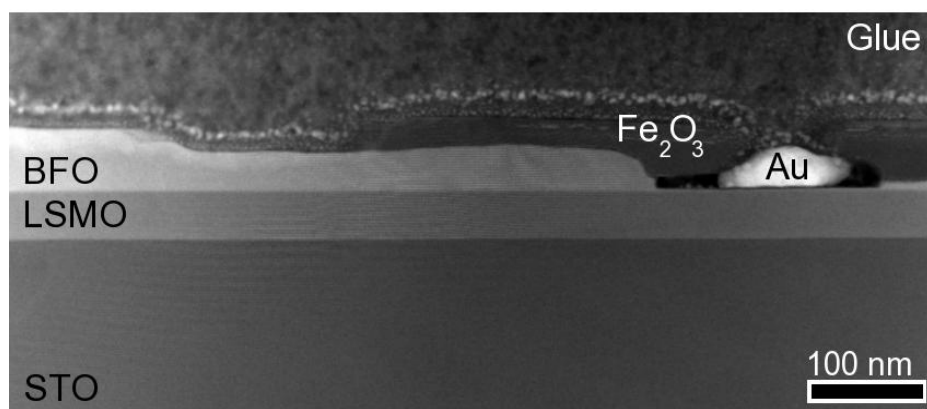
For this study a 50 nm thick BFO layer was deposited on a 50 nm thick  $\text{La}_{0.67}\text{Sr}_{0.33}\text{MnO}_3$  (LSMO) layer, used as a bottom electrode on a  $\text{SrTiO}_3$  (STO) substrate via pulsed laser deposition (PLD). Conditions were deliberately altered (see experimental details) to induce the formation of secondary  $\text{Fe}_2\text{O}_3$  phases. The BFO/LSMO/STO heterostructure was chosen as it couples a multiferroic (BFO) with a ferromagnet electrode (LSMO) on an oxide substrate (STO); this is an oxide system that has garnered significant recent attention [1,12-15]. Figure 1(a) displays the X-ray diffraction (XRD) graph for this sample. It confirms that the desired perovskite BFO, LSMO and STO phases are present in the samples. However, the XRD also shows an extra peak on the right shoulder of the LSMO (002) peak, at  $\sim 49$  degrees, which is identified to be a secondary phase:  $\alpha$ - $\text{Fe}_2\text{O}_3$  (024). Atomic force microscope scans of this sample (Figure 1(b)) reveals that the  $\text{Fe}_2\text{O}_3$  phase forms a criss-cross network of elongated islands nucleated within the BFO matrix.

**Figure 1.** (a) XRD data. The XRD pattern shows an extra peak around  $\sim 49$  degrees that is identified as  $\text{Fe}_2\text{O}_3$ . (b) Atomic force microscope scans of this sample, reveals the  $\text{Fe}_2\text{O}_3$  phase forming a criss-cross network of elongated islands nucleated within the BFO matrix.



Z-contrast imaging for the heterostructure investigated here (Figure 2) indicates that the BFO layer is not uniform but rather has variable thickness; it being 50 nm in the thickest areas and just a few nanometers in the thinnest areas. In regions where the BFO is ultra-thin (or barely present) the region has voids that are occupied by  $\text{Fe}_2\text{O}_3$ . The void shown in the figure also contains gold that has leaked inside from the protective coating that was used for sample preparation for transmission electron microscopy. The voids have a layer of  $\text{Fe}_2\text{O}_3$  surrounding the gold above the BFO layer, which indicates that the  $\text{Fe}_2\text{O}_3$  phase is not uniform. This strongly hints that in those areas, the ablated BFO has broken down into  $\text{Fe}_2\text{O}_3$  and  $\text{Bi}_2\text{O}_3$  (that is likely to have volatilized).

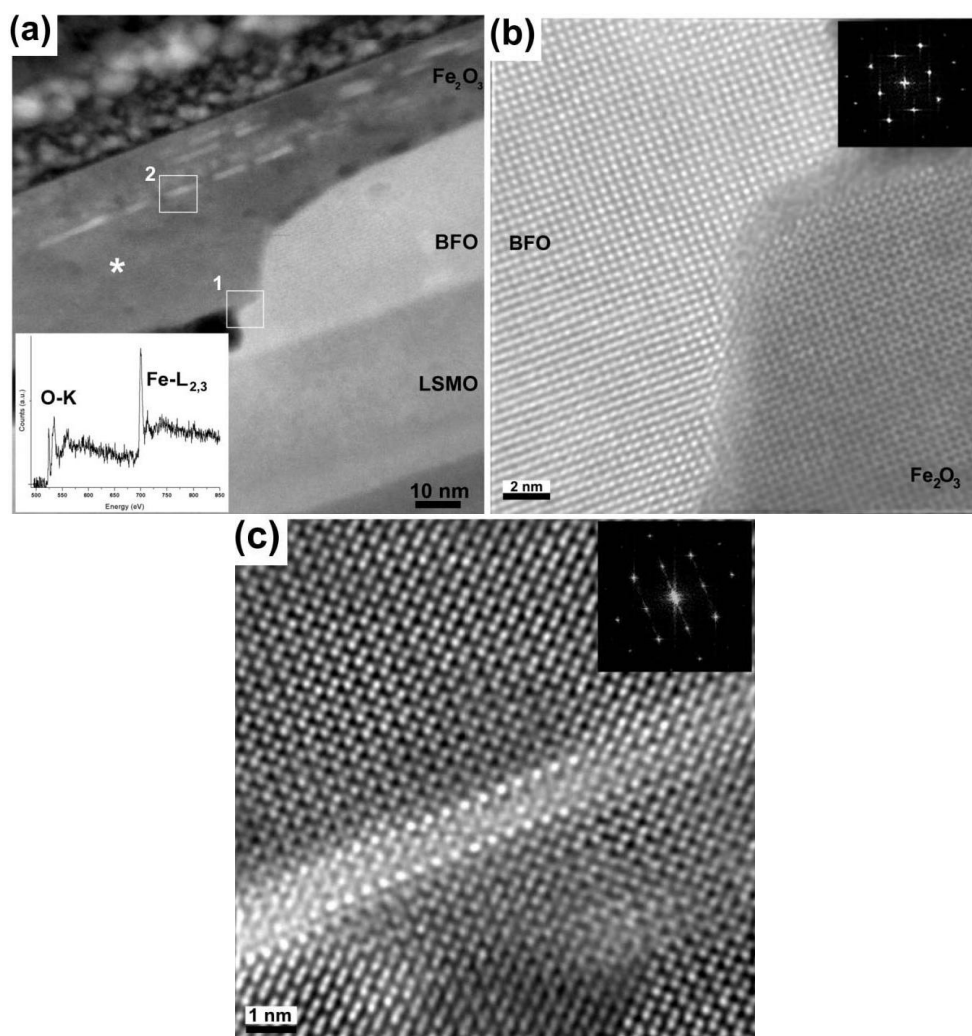
**Figure 2.** [001] Z-contrast overview image.



Electron energy loss spectroscopy (EELS) was performed to confirm that the chemical nature of the layer on top of the BFO, and ascertain that it is indeed the  $\text{Fe}_2\text{O}_3$  found in the XRD pattern (Figure 1(a)). An EEL spectrum (inset in Figure 3(a)) was acquired from the area shown in Figure 3(a) (marked by an asterisk). It shows the two sharp peaks, or ‘white lines’, around 708 eV, which are characteristic of the Fe- $L_{2,3}$  edge as well as a very distinctive O-K edge (onset at about 530 eV), comprising three main peaks. The overall shape and fine structure of these edges match well with those of reference  $\text{Fe}_2\text{O}_3$  spectra, as previously reported by Colliex and Kurata for instance [16-18]. Furthermore the Z-contrast image in Figure 3(a) reveals two distinct areas of interest: The direct interface between the BFO and  $\text{Fe}_2\text{O}_3$  layers (a subset of which is marked as 1 on the figure) and some bright inclusions (marked as 2), located deep within the  $\text{Fe}_2\text{O}_3$  layer that exhibit an intensity level more similar to that of the BFO phase than of the immediately surrounding  $\text{Fe}_2\text{O}_3$ . Figure 3(b) is a high-resolution [001]<sub>BFO</sub> Z-contrast image of Area 1 in Figure 3(a), which corresponds to the interface between the  $\text{Fe}_2\text{O}_3$  and BFO phases. The Fourier transform (shown as an inset) reveals that the two phases appear coherent, indicating epitaxial growth. The diffraction spots resemble those of the BFO [001]. For this particular area, it is suggested that  $\text{Fe}_2\text{O}_3$  adopts the BFO structure due to its proximity to the BFO layer: Both the perovskite-BFO and  $\alpha$ - $\text{Fe}_2\text{O}_3$  have a distorted rhombohedral structure and epitaxial growth is therefore strongly favored. Figure 3(c) on the other hand, is an image of Area 2 containing one of the distinctive inclusions highlighted earlier. While the matrix surrounding the bright inclusion is structurally coherent, it is clearly seen from the image itself that the atomic columns forming the edge of the inclusion are not only brighter but also bigger in size than the surrounding Fe columns, closely matching the intensity and diameter of images of Bi columns acquired at the same

magnification and in the same conditions within the pure BFO region. Furthermore, upon closer inspection, the walls of the inclusion itself do not follow quite the same structure as the surrounding  $\text{Fe}_2\text{O}_3$ , but appear to adopt a tetragonal BFO structure. These observations strongly suggest that the extra phase enclosed within the  $\text{Fe}_2\text{O}_3$  phase is nanoscale BFO inclusions. The Fast Fourier transform of this image (shown as an inset) reveals that even deep inside the  $\text{Fe}_2\text{O}_3$  phase, the structure remains coherent to the bottom BFO layer and the inclusions.

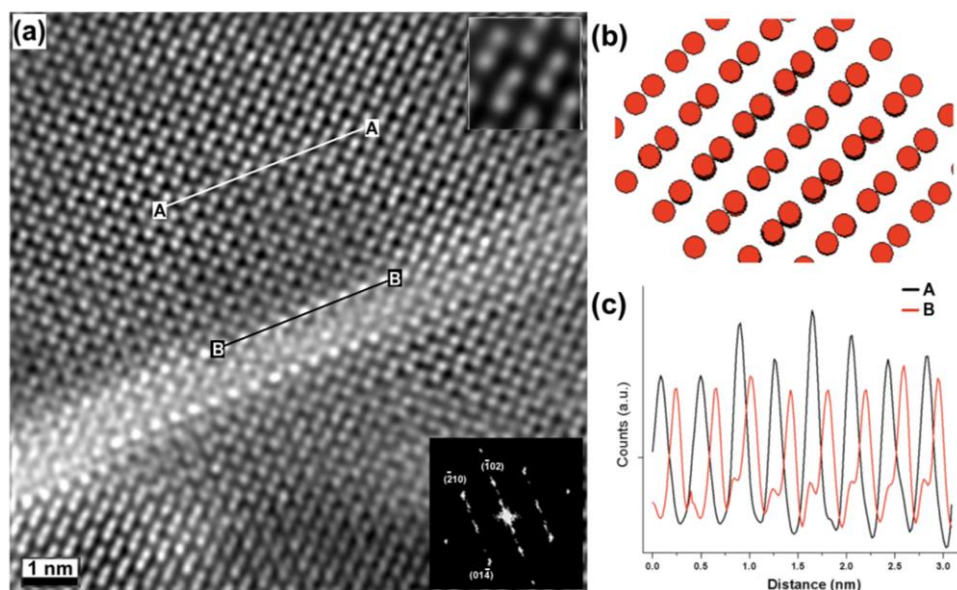
**Figure 3.**  $[001]_{\text{BFO}}$  Z-contrast images. (a) Overview showing the pocket area and the  $\text{Fe}_2\text{O}_3$  layer containing bright inclusions. Its inset contains an EEL spectrum from the area marked by the asterisk, confirming the presence of Fe; (b) Area marked as 1 in (a), showing the BFO and  $\text{Fe}_2\text{O}_3$  merger with their respective diffraction patterns as insets; (c) Area marked as 2 in (a) with its corresponding diffraction pattern, showing an inclusion.



Further high-resolution imaging was performed to investigate how the inclusions are accommodated inside the  $\text{Fe}_2\text{O}_3$  layer. Figure 4(a) shows how the region surrounding the inclusion has a perovskite-like short order structure (a few unit cells) followed by what was determined to be a near- $[241]$   $\alpha\text{-Fe}_2\text{O}_3$  rhombohedral structure (space group  $R\bar{3}c$ ), where the  $\text{Fe}^{3+}$  cations are projected with a doubling structure. A similar case, where the  $\text{Fe}_2\text{O}_3$  phase was also deviated from the  $[001]_{\text{BFO}}$ , has been previously reported by Murakami *et. al.*, [6]. To confirm this structure, a model of the  $\text{Fe}_2\text{O}_3$

structure viewed along the tilted [241] was created using Crystal Maker software (where the  $O^{2-}$  atoms are not represented for clarity purposes), shown in Figure 4(b), where the  $Fe^{3+}$  doubling is observed. It is clear how this model matches the experimental image. Intensity profiles were measured parallel to the inclusion line, along the c-axis, in order to calculate the distance between Fe doublets and the bright atoms (lines marked as A and B in Figure 4(a)), shown in Figure 4(c). The measurements confirmed a distance of  $\sim 0.391$  nm for both cases, which is close to that of BFO (0.396 nm [19,20]). Hence, the mismatch between these two phases is very small ( $\sim 1\%$ ). This now explains how the  $Fe_2O_3$  structure can easily be accommodated on the BFO structure and its predisposition to adopt the lattice arrangement of the ultrathin BFO inclusions, namely the distorted tetragonal structure.

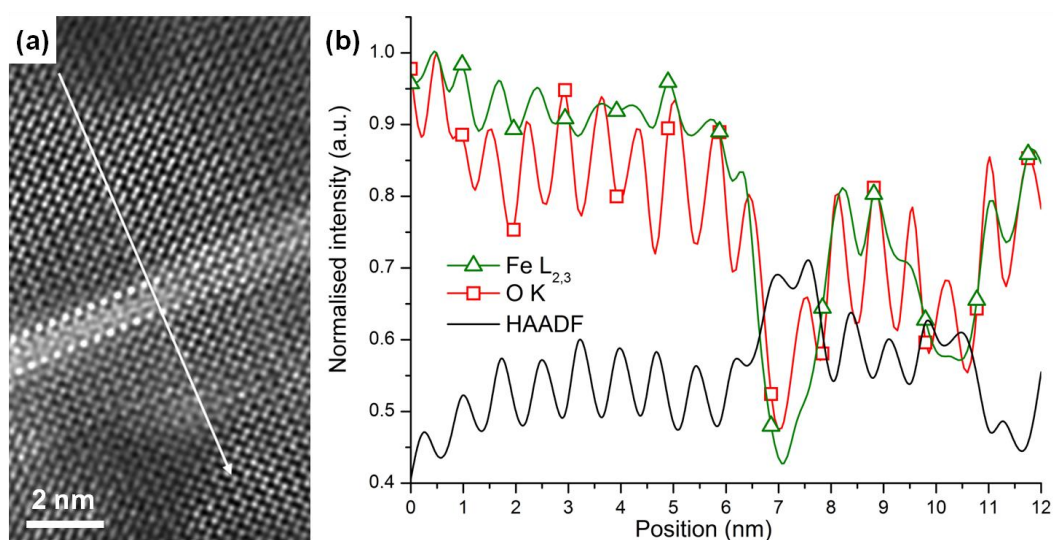
**Figure 4.** (a) Z-contrast image of the  $Fe_2O_3$  phase containing a BFO stripe, the upper inset is a filtered image showing the  $Fe^{3+}$  doubling of the structure. (b) Model of the tilted [241]  $Fe_2O_3$  structure, showing the doubling on the  $Fe^{3+}$  atomic columns. (c) Intensity profiles from (a), measured along the lines marked as A and B.



Point-by-point electron energy loss spectroscopy (EELS) was also performed across the needle-shaped inclusion inside the  $Fe_2O_3$  phase, to gain some insight into its local chemistry. Figure 5(a) is a Z-contrast image of one of the bright inclusions: 50 EEL spectra were acquired serially from top to bottom along a  $\sim 12$  nm line crossing the structure, as indicated on the figure by the white arrow. Figure 5(b) shows the integrated Fe and O EELS intensity as a function of probe position, along with the simultaneously acquired high angular annular dark field (HAADF) signal (green line with triangle markers, red line with square markers, and black solid lines, respectively). The Fe- $L_{2,3}$  edge (res. O-K edge) was integrated over a 60 eV (resp. 50 eV) window above its edge onset. In both cases, the background was removed using a power law model. A striking feature of this intensity profile is the marked intensity decrease in the O-K and Fe- $L_{2,3}$  edges coinciding precisely with the bright needle-shape inclusion, as evidenced by the simultaneous increase in HAADF intensity. This result points to a lower Fe content and/or the presence of oxygen vacancies [18] within the inclusion. Although no EELS spectrum was acquired to confirm categorically the presence of Bi atoms (the Bi-M edge energy

being too high for practical acquisition on the instrument used for this study), the drop in Fe intensity, along with the bright contrast of the atomic columns, strongly suggests that the inclusions are Bi-rich. Combined with our prior structural analysis based on the HAADF images, it is therefore likely that those needle-shaped inclusions mark the thwarted onset of BFO growth, possibly due to a slight change in the pressure/temperature conditions in the PLD chamber.

**Figure 5.** EELS line scan inside the  $\text{Fe}_2\text{O}_3$ , across the stripe. **(a)** Z-contrast image, indicating the points from where the EEL spectra were acquired and **(b)** integrated Fe and O intensity as a function of probe position, along with the simultaneously acquired HAADF signal (green line with triangle markers, red line with square markers and solid black line respectively). The Fe- $L_{2,3}$  edge (res. O-K edge) was integrated over a 60 eV (resp. 50 eV) window above its edge onset. In both cases, the background was removed using a power law model.



### 3. Experimental Section

$\text{BiFeO}_3$  (BFO)/ $\text{La}_{0.67}\text{Sr}_{0.33}\text{MnO}_3$  (LSMO)/ $\text{SrTiO}_3$  (STO) heterostructures were deposited via PLD. The films were deposited at 900 °C, 100 mTorr  $\text{O}_2$  with a laser fluence of  $2 \text{ J}\cdot\text{cm}^{-2}$  for LSMO and 900 °C, 10 m Torr  $\text{O}_2$  with a laser fluence of  $1.6 \text{ J}\cdot\text{cm}^{-2}$  and a frequency of 10 Hz, then cooled at  $20^\circ \text{ min}^{-1}$  under a 200 Torr  $\text{O}_2$  atmosphere.

Cross-sectional TEM samples were prepared by standard mechanical tripod polishing and ion beam thinning procedures [21]. The samples were gold-coated prior to TEM sample preparation in order to protect the top layer. Except where otherwise specified, Z-contrast imaging and electron energy loss spectroscopy (EELS) were carried out using an aberration-corrected, dedicated STEM VG HB UX operated at 100kV and equipped with an Enfina parallel EELS detector. For all data presented here, the beam convergence semi-angle was 21 mrad with HAADF detector inner and outer radii of 70 and 210 mrad, respectively. Z-contrast images were used to position the  $\sim 1 \text{ \AA}$  probe on specific atomic positions or line scans, with a dispersion of 0.2 to 0.3 eV per channel and a collection semi-angle of 19 mrad. Except where specified, Z-contrast image were processed using a probe deconvolution algorithm based on maximum entropy methods in order to minimize the noise levels [22].

#### 4. Conclusions

The interfacial structure and chemistry of secondary Fe<sub>2</sub>O<sub>3</sub> phase found in BFO/LSMO heterostructure is investigated. HRTEM and STEM images reveal that Fe<sub>2</sub>O<sub>3</sub> pockets can be easily accommodated by the host BFO phase, due to a similar crystallographic structure and close epitaxial registry. The observation of Fe-deficient bright needle-shaped inclusions within the Fe<sub>2</sub>O<sub>3</sub> phase also suggests that minute changes in the growth conditions could trigger BFO growth, although in our case this growth was not sustained. This, combined with previously mentioned structural similarity, could explain why Fe<sub>2</sub>O<sub>3</sub> is so easily formed during BFO thin film synthesis, and possibly open new routes for creating hybrid nanoscale Fe<sub>2</sub>O<sub>3</sub>-BFO heterostructures.

#### Acknowledgements

Part of this work was performed at the National Center for Electron Microscopy, which is supported by the Office of Science, Office of Basic Energy Sciences of the U.S. Department of Energy under Contract No. DE-AC02—05CH11231. V.N and M.A also acknowledge support from the ARC Discovery Program.

#### References

1. Ramesh, R.; Spaldin, N.A. Multiferroics: Progress and prospects in thin films. *Nat. Mater.* **2007**, *6*, 21-29.
2. Bea, H.; Bibes, M.; Zhu, X.H.; Fusil, S.; Bouzheouane, K.; Petit, S.; Kreisel, J.; Barthelemy, A. Crystallographic, magnetic, and ferroelectric structures of bulklike BiFeO<sub>3</sub> thin films. *Appl. Phys. Lett.* **2008**, *93*, 072901-072903.
3. Kan, D.; Palova, L.; Anbusathaiah, V.; Cheng, C.J.; Fujino, S.; Nagarajan, V.; Rabe, K.M.; Takeuchi, I. Universal behavior and electric-field-induced structural transition in rare-earth-Substituted BiFeO<sub>3</sub>. *Adv. Funct. Mater.* **2010**, *20*, 1108-1115.
4. Zeches, R.J.; Rossell, M.D.; Zhang, J.X.; Hatt, A.J.; He, Q.; Yang, C.H.; Kumar, A.; Wang, C.H.; Melville, A.; Adamo, C.; Sheng, G.; Chu, Y.H.; Ihlefeld, J.F.; Erni, R.; Ederer, C.; Gopalan, V.; Chen, L.Q.; Schlom, D.G.; Spaldin, N.A.; Martin, L.W.; Ramesh, R. A strain-driven morphotropic phase boundary in BiFeO<sub>3</sub>. *Science* **2009**, *326*, 977-980.
5. Anbusathaiah, V.; Cheng, C.J.; Lim, S.H.; Murakami, M.; Salamanca-Riba, L.G.; Takeuchi, I.; Nagarajan, V. Role of oxygen partial pressure and seed layer chemistry in flux mediated epitaxy of single phase multiferroic BiFeO<sub>3</sub> thin films. *Appl. Phys. Lett.* **2008**, *93*, 192906.
6. Bea, H.; Bibes, M.; Barthelemy, A.; Bouzheouane, K.; Jacquet, E.; Khodan, A.; Contour, J.P.; Fusil, S.; Wyczisk, F.; Forget, A.; Lebeugle, D.; Colson, D.; Viret, M. Influence of parasitic phases on the properties of BiFeO<sub>3</sub> epitaxial thin films. *Appl. Phys. Lett.* **2005**, *87*, doi: 10.1063/1.2009808.
7. Murakami, M.; Fujino, S.; Lim, S.H.; Salamanca-Riba, L.G.; Wuttig, M.; Takeuchi, I.; Varughese, B.; Sugaya, H.; Hasegawa, T.; Lofland, S.E. Microstructure and phase control in Bi-Fe-O multiferroic nanocomposite thin films. *Appl. Phys. Lett.* **2006**, *88*, 112505.

8. Ramakrishnan, S.; Arredondo, M.; Saunders, M.; Ramasse, Q.M.; Valanoor, N.; Munroe, P. Microstructural analysis of ferromagnetic-multiferroic epitaxial heterostructure interfaces. *J. Appl. Phys.* **2010**, in press.
9. Lim, S.H.; Murakami, M.; Yang, J.H.; Young, S.Y.; Hattrick-Simpers, J.; Wuttig, M.; Salamanca-Riba, L.G.; Takeuchi, I. Enhanced dielectric properties in single crystal-like BiFeO<sub>3</sub> thin films grown by flux-mediated epitaxy. *Appl. Phys. Lett.* **2008**, *92*, 012918.
10. Qi, X.D.; Dho, J.; Tomov, R.; Blamire, M.G.; MacManus-Driscoll, J.L. Greatly reduced leakage current and conduction mechanism in aliovalent-ion-doped BiFeO<sub>3</sub>. *Appl. Phys. Lett.* **2005**, *86*, 062903.
11. Eerenstein, W.; Morrison, F.D.; Dho, J.; Blamire, M.G.; Scott, J.F.; Mathur, N.D. Comment on epitaxial BiFeO<sub>3</sub> multiferroic thin film heterostructures. *Science* **2005**, *307*, 1203.
12. Borisevich, A.Y.; Chang, H.J.; Huijben, M.; Oxley, M.P.; Okamoto, S.; Niranjana, M.K.; Burton, J.D.; Tsymbal, E.Y.; Chu, Y.H.; Yu, P.; Ramesh, R.; Kalinin, S.V.; Pennycook, S.J. Suppression of octahedral tilts and associated changes in electronic properties at epitaxial oxide heterostructure interfaces. *Phys. Rev. Lett.* **2010**, *105*, 087204.
13. Yu, P.; Lee, J.S.; Okamoto, S.; Rossell, M.D.; Huijben, M.; Yang, C.H.; He, Q.; Zhang, J.X.; Yang, S.Y.; Lee, M.J.; Ramasse, Q.M.; Erni, R.; Chu, Y.H.; Arena, D.A.; Kao, C.C.; Martin, L.W.; Ramesh, R. Interface ferromagnetism and orbital reconstruction in BiFeO<sub>3</sub>-La<sub>0.7</sub>Sr<sub>0.3</sub>MnO<sub>3</sub> heterostructures. *Phys. Rev. Lett.* **2010**, *105*, 027201:1-027201:5.
14. Borisevich, A.Y.; Ovchinnikov, O.S.; Chang, H.J.; Oxley, M.P.; Yu, P.; Eliseev, E.A.; Morozovska, A.N.; Ramesh, R.; Pennycook, S.J.; Kalinin, S.V. Mapping octahedral tilts and polarization across a domain wall in BiFeO<sub>3</sub> from Z-contrast scanning transmission electron microscopy image atomic column shape analysis. *ACS Nano* **2010**, in press.
15. Hambe, M.; Petraru, A.; Pertsev, N.A.; Munroe, P.; Nagarajan, V.; Kohlstedt, H. Crossing an interface: Ferroelectric control of tunnel currents in magnetic complex oxide heterostructures. *Adv. Funct. Mater.* **2010**, *20*, 2436-2441.
16. Colliex, C.; Manoubi, T.; Ortiz, C. Electron-energy-loss-spectroscopy near-edge fine-structures in the iron-oxygen system. *Phys. Rev. B* **1991**, *44*, 11402-11411.
17. Kurata, H.; Lefevre, E.; Colliex, C.; Brydson, R. Electron-energy-loss near-edge structures in the oxygen K-edge spectra of transition-metal oxides. *Phys. Rev. B* **1993**, *47*, 13763-13768.
18. Lee, Y.C.; Chueh, Y.L.; Hsieh, C.H.; Chang, M.T.; Chou, L.J.; Wang, Z.L.; Lan, Y.W.; Chen, C.D.; Kurata, H.; Isoda, S. p-Type alpha-Fe<sub>2</sub>O<sub>3</sub> nanowires and their n-Type transition in a reductive ambient. *Small* **2007**, *3*, 1356-1361.
19. Jang, H.W.; Ortiz, D.; Baek, S.H.; Folkman, C.M.; Das, R.R.; Shafer, P.; Chen, Y.; Nelson, C.T.; Pan, X.; Ramesh, R.; Eom, C.B. Domain engineering for enhanced ferroelectric properties of epitaxial (001) BiFeO thin films. *Advan. Mater.* **2009**, *21*, 817-823.
20. Qi, X.D.; Wei, M.; Lin, Y.; Jia, Q.X.; Zhi, D.; Dho, J.; Blamire, M.G.; MacManus-Driscoll, J.L. High-resolution X-ray diffraction and transmission electron microscopy of multiferroic BiFeO<sub>3</sub> films. *Appl. Phys. Lett.* **2005**, *86*, 071913.
21. Williams, D.B.; Carter, C.B. *Transmission Electron Microscopy*; Plenum Press: New York, NY, USA, 1996; p. 729.

22. Ishizuka, K.; Abe, E. Improvement of spatial resolution of STEM-HAADF image by maximum-entropy and Richardson-Lucy Deconvolution. In *Proceedings of the 13th European Microscopy Congress (13th EMC) Instrumentation and Method*, Antwerp, Belgium, 22–27 August 2004; volume 1, p. 117.

© 2010 by the authors; licensee MDPI, Basel, Switzerland. This article is an open access article distributed under the terms and conditions of the Creative Commons Attribution license (<http://creativecommons.org/licenses/by/3.0/>).